ISPRS Journal of Photogrammetry and Remote Sensing 80 (2013) 72–79

Contents lists available at SciVerse ScienceDirect

ISPRS Journal of Photogrammetry and Remote Sensing

journal homepage: www.elsevier.com/locate/isprsjprs

Improved topographic mapping through high-resolution SAR interferometry with atmospheric effect removal

Mingsheng Liao [a], Houjun Jiang [a], Yong Wang [b,a], Teng Wang [a], Lu Zhang [a,*]

[a] State Key Laboratory of Information Engineering in Surveying, Mapping and Remote Sensing, Wuhan University, 129 Luoyu Road, Wuhan 430079, PR China
[b] Department of Geography, East Carolina University, Greenville, NC 27858, USA

ARTICLE INFO

Article history:
Received 14 April 2012
Received in revised form 17 March 2013
Accepted 25 March 2013

Keywords:
High-resolution,
SAR interferometry
Topographic mapping
SRTM
Atmospheric stratification
Atmospheric turbulence

ABSTRACT

The application of SAR interferometry (InSAR) in topographic mapping is usually limited by geometric/temporal decorrelations and atmospheric effect, particularly in repeat-pass mode. In this paper, to improve the accuracy of topographic mapping with high-resolution InSAR, a new approach to estimate and remove atmospheric effect has been developed. Under the assumptions that there was no ground deformation within a short temporal period and insignificant ionosphere interference on high-frequency radar signals, e.g. X-bands, the approach was focused on the removal of two types of atmospheric effects, namely tropospheric stratification and turbulence. Using an available digital elevation model (DEM) of moderate spatial resolution, e.g. Shuttle Radar Topography Mission (SRTM) DEM, a differential interferogram was firstly produced from the high-resolution InSAR data pair. A linear regression model between phase signal and auxiliary elevation was established to estimate the stratified atmospheric effect from the differential interferogram. Afterwards, a combination of a low-pass and an adaptive filter was employed to separate the turbulent atmospheric effect. After the removal of both types of atmospheric effects in the high-resolution interferogram, the interferometric phase information incorporating local topographic details was obtained and further processed to produce a high-resolution DEM. The feasibility and effectiveness of this approach was validated by an experiment with a tandem-mode X-band COSMO-SkyMed InSAR data pair covering a mountainous area in Northwestern China. By using a standard Chinese national DEM of scale 1:50,000 as the reference, we evaluated the vertical accuracy of InSAR DEM with and without atmospheric effects correction, which shows that after atmospheric signal correction the root-mean-squared error (RMSE) has decreased from 13.6 m to 5.7 m. Overall, from this study a significant improvement to derive topographic maps with high accuracy has been achieved by using the proposed approach.

1. Introduction

The repeat-pass mode is widely employed to acquire the InSAR data pair. However, the application of repeat-pass InSAR in topographic mapping is usually limited by geometric/temporal decorrelations and atmospheric effects. In order to minimize the adverse impacts of geometric/temporal decorrelations, SAR satellite constellations such as ERS-1/2 or COSMO-SkyMed were formed and operated (Rufino et al., 1998; Covello et al., 2010). In the tandem mode, a short revisit period of only one day or less can be achieved, which would minimize the temporal decorrelation. However, it brings the atmospheric artifacts to be a major problem in repeat-pass InSAR topographic mapping (Ferretti et al., 1999; Crosetto, 2002).

The atmosphere between SAR sensor and ground targets usually varies across the spatial coverage of SAR data. In addition, temporal variation of the atmosphere always exists between two passes. Both variations can adversely influence the accuracy of the InSAR-derived DEM. The contribution of the atmospheric effect is mainly due to the troposphere and the ionosphere. The radar signal is delayed when passing through the troposphere. Temporal change of radar signal delay can introduce significant errors. For example, a temporal change of 20% in the relative humidity of the troposphere could lead to a vertical error up to 100 m (Zebker et al., 1997). The ionosphere interference is inversely proportional to the square of radar frequency, hence for the X-band (9.6 GHz) data used in this study, the ionospheric effect could be minimal or be ignored (Hanssen, 2001; Brcic et al., 2011).

To remove the atmospheric effect in DEM production using repeat-pass InSAR data, researchers have explored the multi-baseline InSAR, times series InSAR, e.g. Permanent Scatterer InSAR

* Corresponding author.
E-mail address: luzhang@whu.edu.cn (L. Zhang).

0924-2716/$ - see front matter © 2013 International Society for Photogrammetry and Remote Sensing, Inc. (ISPRS) Published by Elsevier B.V. All rights reserved.
http://dx.doi.org/10.1016/j.isprsjprs.2013.03.008

(PSInSAR™) (Ferretti et al., 2001), and auxiliary data based methods. For the multi-baseline InSAR method, multiple interferograms are merged using a weighted average or a joint estimation (Knöpfle et al., 1998; Ferraiuolo et al., 2009). During the merging, the atmospheric effect from each observation is assumed to be independent and randomly distributed temporally. The averaging process can reduce the atmospheric effect, whenever the number of observations is large enough. The PSInSAR approach can generally achieve submeter DEM accuracy for deformation mapping, but it requires numerous repetitive observations, typically more than 20 scenes (Ferretti et al., 2001). The accurate estimation of the height is achieved at the location where there is a permanent scatterer. Interpolation is needed for the correction of the atmospheric effect within an area of interest. Thus, a large number of permanent scatterers per unit area is critical. The high-density requirement is hardly met especially in mountainous areas. The methods based on auxiliary data such as water vapor product from multispectral remote sensing data can achieve nearly 20–40% improvement of the accuracy of the InSAR-derived DEM (Ding et al., 2008). However, the water vapor product is only useful under a cloud free condition, and few multispectral sensors (nadir-looking) can work simultaneously with SAR (side-looking).

In this paper an alternative approach to remove the atmospheric effect has been developed for high-resolution DEM generation under the conditions that only an interferogram of high-resolution and an SRTM DEM of moderate resolution are available. In particular, with the requirement of a short temporal baseline we reasonably assume no ground surface deformation. Using the SRTM DEM, we derive a differential interferogram from the high-resolution InSAR data pair. Phase information in such a differential interferogram is comprised of not only local topographic details, but also the temporal difference of atmospheric effects between two passes. By fully exploiting the characteristics of spatial-temporal distribution patterns of topographic and atmospheric phase signals, a two-stage approach is developed to separate atmospheric phase components from the differential interferogram. As a result, refined topographic phase information is obtained, and finally the high-resolution DEM can be generated.

2. Methodology

2.1. Phase in the differential interferogram

The phase of a resolution cell in the differential interferogram or interferogram for short can be decomposed as five components (Ferretti et al., 2001),

$$\phi_{\text{diff}} = \phi_{\varepsilon\text{topo}} + \phi_{\text{atm}} + \phi_{\text{def}} + \phi_{\text{orbit}} + \phi_{\text{noise}} \quad (1)$$

where $\phi_{\varepsilon\text{topo}}$ is the topographic phase that is mainly caused by the height error in the inaccurate auxiliary DEM. $\phi_{\varepsilon\text{topo}}$ is the information useful for us to derive the high-resolution DEM. The rest of the phase terms are undesirable and should be removed in order to produce accurate DEM products. Particularly, ϕ_{atm} is the phase contributed from the atmospheric phase screen (APS), which is caused by the change of radar signal delay between two acquisitions. ϕ_{def} is related to the ground deformation, which can be ignored in topographic mapping with an InSAR pair of a favorite temporal baseline, e.g. one or several days. ϕ_{orbit} is the phase due to orbit error. It is usually shown as a systematic phase trend that can be removed by height calibration (Ferretti et al., 2001; Liao et al., 2007). ϕ_{noise} is the phase caused by noise such as the decorrelation between the InSAR pair and thermal noise of the SAR sensor. It can be greatly reduced through interferogram filtering (Goldstein, 1998). Hence, the contribution from ϕ_{def}, ϕ_{orbit} and ϕ_{noise} can be significantly reduced or ignored, which let only ϕ_{atm} remain.

2.2. Estimation of the atmospheric effect

It has been suggested by Hanssen (2001) that the atmospheric effects in a SAR interferogram can be categorized into vertical stratification and turbulence mixing. Thus, ϕ_{atm} can be decomposed as a stratification component and a turbulent one. Based on the physical and statistic properties, a phase-to-elevation regression and a spectral filtering are proposed to estimate and remove these two APS components separately.

2.2.1. Estimation of the stratification effect

The phase delay caused by vertical stratifications of atmosphere is determined by the refractivity profile along the path of radar wave propagation. With the assumption of a horizontally homogeneous atmosphere within an area of interest and a zenith refractivity of $N(z)$ as a function of altitude z, the phase delay of acquisition i can be written as (Hanssen, 2001)

$$\phi_i = \frac{4\pi}{\lambda \cos\theta} 10^{-6} \int_h^\infty N_i(z)dz \quad (2)$$

Therefore, the stratified APS ϕ_{strat} is related to the difference of $N(z)$ between acquisitions i and j as

$$\phi_{\text{strat}} = \phi_i - \phi_j = \frac{4\pi}{\lambda\cos\theta} 10^{-6} \int_h^\infty (N_i(z) - N_j(z))dz = \frac{4\pi}{\lambda\cos\theta} 10^{-6} \int_h^\infty \Delta N(z)dz \quad (3)$$

where h is the elevation value of the ground target, λ is the radar wavelength, and θ is the radar look angle. Clearly, ϕ_{strat} is a function of h and it is highly correlated with topography. Since the zenith refractivity difference $\Delta N(z)$ is typically not available, ϕ_{strat} cannot be directly estimated using Eq. (3). Alternatively, we estimate ϕ_{strat} within the interferogram by a linear model (Chaabane et al., 2007; Doin et al., 2009) between stratified APS ϕ_{strat} and elevation h as

$$\phi_{\text{strat}} = kh + c \quad (4)$$

With the assumption that the observed phase (ϕ_{obs}) of the interferogram is ϕ_{strat}, h can be derived from the reference SRTM DEM. The estimation of phase-elevation ratio k is a key step and can be considered as an optimization problem defined by an objective function in the form of

$$k = \arg\max \left\{ \left| \sum_i \rho_i \exp\{j(\phi_{\text{obs},i} - kh_i)\} \right| \right\} \quad (5)$$

where subscript i indicates the i-th observation or sample ($i = 1, 2, \ldots, n$). The magnitude of coherence, ρ_i is used as the weight for the i-th sample in the regression. To avoid phase unwrapping we performed the optimization in the complex domain as suggested by Chaabane et al. (2007). In general, an optimal solution can be obtained using the generalized pattern search algorithm that does not require any information about the gradient of the objective function (Audet and Dennis, 2003). More importantly, as shown in Section 3.2, the strategy was able to derive satisfactory results. After the estimation of parameter k, the constant term c in Eq. (4) can be obtained by simply computing the phase of the complex sum in Eq. (5).

2.2.2. Estimation of the turbulence effect

Turbulent mixing resulted from turbulent processes in the troposphere will cause three dimensional (3D) spatial heterogeneity and temporal variability in the refractivity, and it happens in both flat and mountainous areas. The turbulence effect can be characterized by the power spectrum after the spatial Fourier transform applied to the interferogram (Hanssen, 2001). The spectrum reveals the energy distribution of the effect at different spatial scales. Hanssen (1998) analyzed a set of 26 differential interferograms from ERS tandem interferometry, and found that the spectra of

the interferograms following a power-law of −5/3 for a spatial extent larger than 2 km, −8/3 for an area between 0.5 km and 2 km, and −2/3 for a spatial extent less than 0.5 km. For spatial extents larger than 0.5 km, the power-law structure is from turbulence effect, while for those smaller than 0.5 km the structure is likely from the SRTM DEM error and decorrelation rather than atmospheric turbulence (Hanssen, 2001). Therefore, in the differential interferogram the turbulent APS ϕ_{atm} is a low-frequency signal, while topographic phase $\phi_{\varepsilon\text{topo}}$ is a high-frequency one. Since the APS from troposphere is independent of radar wavelength, the X-band interferogram in this study should show a similar phenomenon as observed from C-band ERS data (Hanssen, 1998).

According to the spectral characteristics mentioned above, we estimate the turbulence effect by using a frequency filter $G(u, v)$ composed of a low-pass filter $L(u, v)$ and an adaptive filter $H(u, v)$. u, v are azimuth and range variables or indices in the spatial frequency domain, respectively. Both filters $L(u, v)$ and $H(u, v)$ work together in the estimation of turbulence effect and they share the same input samples. It should be noted that the filter $G(u, v)$ is originally proposed by Hooper (2006), and is used to extract spatially correlated phase with the Stanford Method for Persistent Scatterers (StaMPS). In StaMPS, $G(u, v)$ is implemented as $[L(u, v) + p(H(u, v)/H^*(u, v) - 1)^q]$. Coefficients p and q vary between 0 and 1. Both p and q are empirically determined. $H(u, v)$ is an adaptive filter that determines the pass band based on the dominant frequencies of input. It is defined as

$$H(u, v) = |S(u, v)| \tag{6}$$

where S is a two-dimensional Fourier transform of complex differential phase (Goldstein and Werner, 1998). $H^*(u, v)$ is the median value of $H(u, v)$. Negative values of $(H(u, v)/H^*(u, v) - 1)$ are set to zero in Hooper's implementation. This operation reduces the bandwidth of $H(u, v)$ and may result in over-smoothing. To preserve the bandwidth of $H(u, v)$, we modify the filter $G(u, v)$ as

$$G(u, v) = L(u, v) + p\left(\frac{H(u, v)}{\max(H(u, v))}\right)^q \tag{7}$$

The low-pass filter $L(u, v)$ is used to estimate the turbulence effect with a spatial extent larger than the thickness of the turbulent layer, i.e. about 2 km, which is the depth of the convective boundary layer (Hanssen, 2001). Then, the cutoff value of the spatial frequency of $L(u, v)$ is set as 0.5 cycle/km. The adaptive filter $H(u, v)$ is used to estimate the turbulence effect with a spatial extent smaller than 2 km, which are the dominate signals in a local area of 2×2 km^2. The interferogram is then divided into consecutive subareas of 2×2 km^2. The response of $H(u, v)$ is calculated from each subarea using Eq. (6) so that the bandwidth based on the local atmospheric signals was adaptively determined. The coefficient pair (p, q) can be empirically determined through a trial-and-error approach. However, as discussed later in Section 4, the choice of a non-zero pair (p, q) might be not so critical in the use of filter $G(u, v)$ in each subarea. Therefore, for the purpose of simplifying calculation, we use $p = q = 1.0$ in the estimation of the effect of the atmospheric turbulence on the phase, and discuss possible consequences.

2.3. Study area and datasets

The study area is about 10×10 km^2 in the Qilian Mountains, located in the northwestern part of China (39°35′N and 96°27′E). The elevation varies from 3100 to 4300 m above the mean sea level. The area is near the north of the Mengke Glacier. It has a landform of mountains with steep slopes, and glacial fluvial deposition near the foot of the mountains. This place is a good candidate for InSAR topographic mapping because it is remote and diverse in relief types. In addition, the elevation in most parts of the study site is below the snow line of about 4267 m, and the InSAR data pair is acquired in June. Thus, the snow and ice cover should be minimal. Therefore, the impact of glacier dynamics on topographic mapping could be marginal or be ignored.

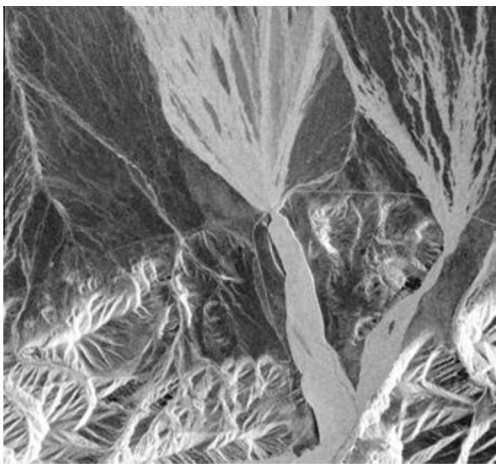

Fig. 1. The amplitude image of COSMO-SkyMed data acquired on 3 June 2009.

An InSAR image pair was acquired by COSMO-SkyMed on 3 June 2009 and 4 June 2009. The nominal resolution of the SAR data was 3 m in ground range. The normal baseline of the pair was about 63 m resulting in a height of ambiguity being −164 m. Fig. 1 shows the amplitude image. Two fan-shaped glacial fluvial deposits were clearly shown and located near top-middle and top-right. Two tracks of the accumulation and ablation zones (a V-shape) were near the bottom toward right.

The reference DEM was the SRTM DEM with a spatial resolution of 3 arcsecond or about 90 m with a circular absolute geo-location error within ±8.8 m for individual cells. The linear vertical absolute height error in Eurasia was declared to be within ±6.2 m, but the error depends on the topography (Rodriguez et al., 2006). The DEM provided an estimation of the elevation for the area at a moderate resolution, and was further used to simulate an interferogram as mentioned previously. Due to the difference in resolution between the real and simulated interferograms, the differential interferogram obtained exhibited a great deal of phase information partially corresponding to local topographic variations that could not be rendered by the SRTM DEM. As the InSAR data pair was acquired only one-day apart, we can reasonably assume that there was no ground surface deformation within the study area. Therefore, with the APS estimated and removed from the differential interferogram, we can produce high-resolution DEM with the combined use of high-resolution InSAR data and SRTM DEM. Furthermore, the accuracy assessment for the resulting DEM can be used to verify the effectiveness of the proposed method for APS removal.

For the accuracy assessment for the high resolution DEM, a standard Chinese national DEM of scale 1:50,000 provided by the National Geomatics Center of China is used as the reference data. This DEM was produced in 2007 by aerial photogrammetry coupled with GCP measurements. It has a spatial resolution of 25 m. Its vertical error is specified to be within ±10 m. The 1:50,000 DEM is currently the finest DEM over the study area available in China.

3. Experimental results

3.1. Differential interferogram

With the COSMO-SkyMed InSAR data pair, an interferogram was created. To reduce the noise in the interferogram, we multi-looked it by a factor of 3 in both azimuth and range

dimensions. Thus, the nominal spatial resolution of the interferogram was 9 m. Then, after the removal of the reference phase of earth ellipsoid, the interferogram was superimposed on the SAR amplitude data and shown in Fig. 2a. A gradual variation of the phase in the interferogram occurred in the top part where glacial fluvial deposition exists. A rapid phase change was mainly near the bottom where the terrain is rugged and the relief is large. The SRTM DEM was used to simulate another interferogram within the study area. Fig. 2b is the overlay of the interferogram to the same amplitude image. When compared with the real interferogram, the simulated one might lack high-frequency components or there was some loss of details due to the moderate resolution. However, in both interferograms, major spatial patterns were similar or there was a strong agreement in the components of low spatial frequency.

Applying a difference operation to both interferograms, we obtained the differential one. Again, with the same amplitude data as background, the result is given in Fig. 2c. Overall, the interferogram resembles the amplitude data (Fig. 1) that renders topographic features due to the side-looking geometry of SAR imaging. Also, because of the presence of stratified APS, ϕ_{strat} in Eq. (3) is highly correlated with the elevation. The stratified APS dominates the differential interferogram and could obscure the atmospheric turbulence and topographic phase $\phi_{\varepsilon\text{topo}}$.

3.2. Estimation and correction of the stratified APS

To estimate the stratified APS, we extracted cells with high coherence from the differential interferogram as they are less affected by the phase noise caused by decorrelations as well as thermal noises of the SAR system. In addition, elevation values of the cells were extracted from the SRTM DEM. Then, a scatterplot of the differential interferometric phase and elevation data was obtained, as shown in Fig. 3a. There was a clear linear relationship between both variables. Because the regression of Eq. (4) was performed using the nonlinear wrapped phase data, an iterative procedure was needed to estimate the intercept and slope parameters. With the generalized pattern search algorithm (Audet and Dennis, 2003), a linear model that meets requirements of Eq. (5) was obtained as

$$\phi_{\text{strat}} = -0.010094h + 1.280681 \tag{8}$$

After the phase wrapping, the model was plotted as the solid lines in Fig. 3a. There was a good fit of the data overall with some exceptions. For instance, when the elevation value was over 4100 m the fit of the model to the data may fall apart. Such an exception could be attributed to the turbulent APS in high mountains. Rapid change in elevation could make atmospheric turbulence severe.

With Eq. (8) and elevation data from the SRTM DEM, ϕ_{strat} was modeled within the entire study area. The overlay of ϕ_{strat} on the amplitude image was shown in Fig. 3b. The phase value was rewrapped, and the spatial pattern of stratified APS was very similar to that of the differential interferogram shown in Fig. 2c. In other words, the similarity supports that the stratified APS dominated as stated above. Subtracting ϕ_{strat} from the differential interferogram, we obtained the interferometric phase without the stratified APS (Fig. 3c). Obviously, the turbulent APS was revealed, and $\phi_{\varepsilon\text{topo}}$

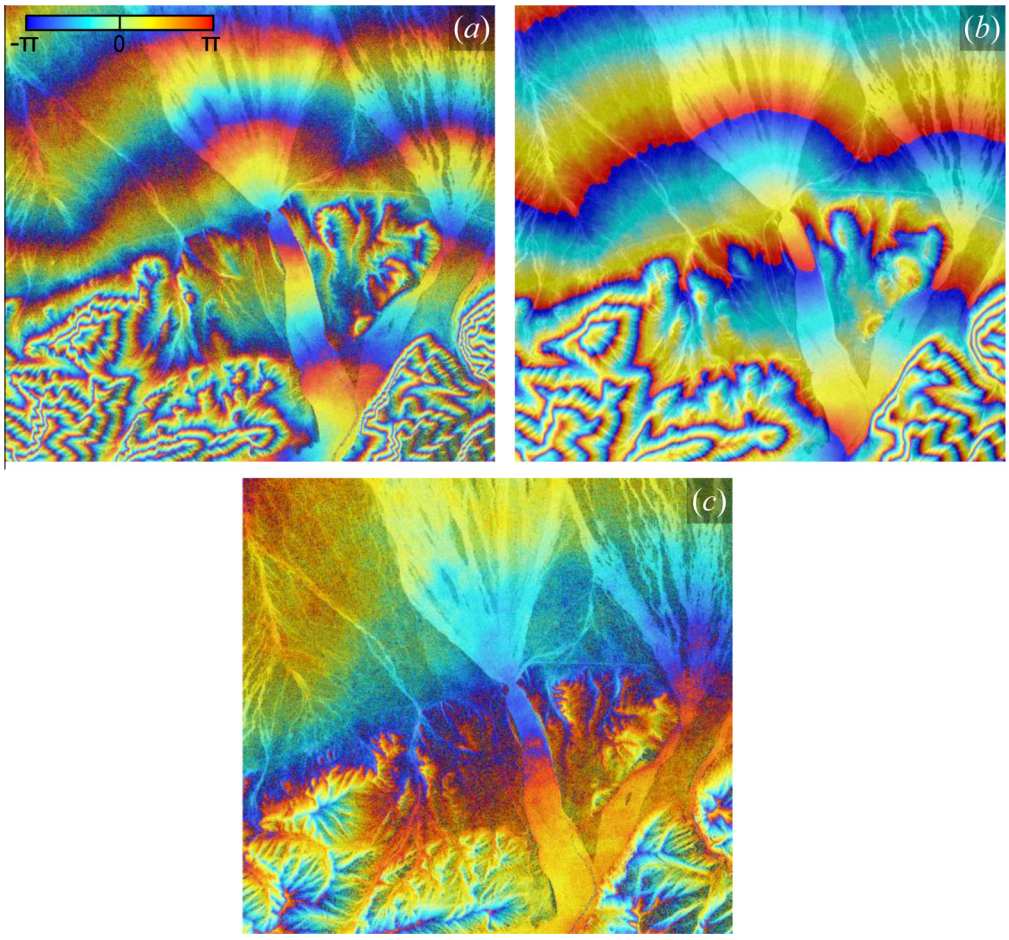

Fig. 2. Overlays on a SAR amplitude image using (a) interferogram of InSAR pair, (b) interferogram simulated from SRTM DEM, and (c) differential interferogram.

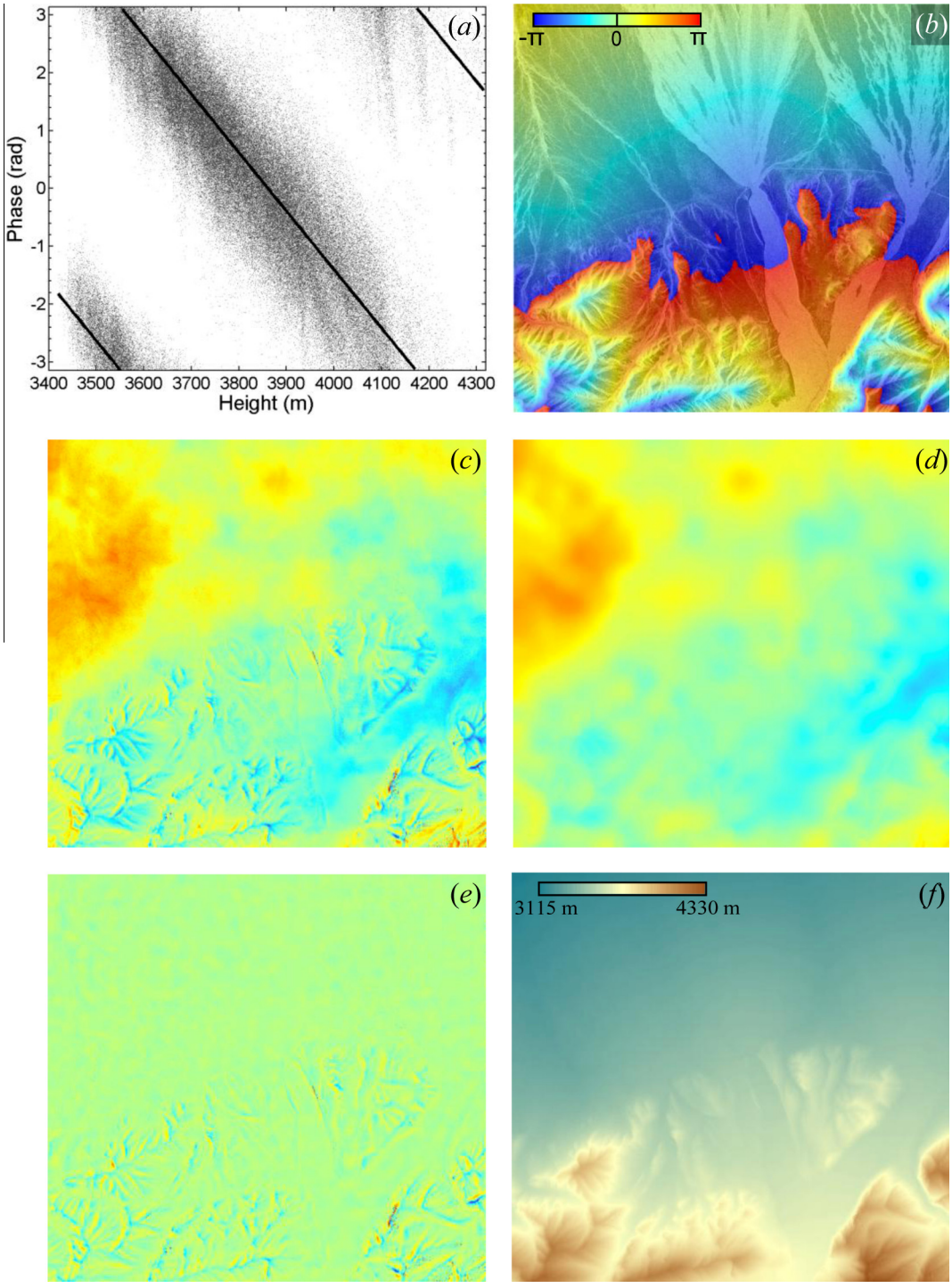

Fig. 3. Estimation and correction of atmospheric effects, and DEM in SAR coordinate system. (a) A scatterplot of the differential phase as a function of elevation. (b) Modeled stratified APS superimposed on SAR data. (c) Interferogram after removal of stratified APS. (d) Estimated turbulent APS. (e) Interferogram after removal of both stratified and turbulent APS and (f) InSAR derived high-resolution DEM after APS correction.

could also be highlighted. It is noteworthy that the phase image after the removal of stratified APS cannot be overlaid on the amplitude image because both data contain detailed topographic information.

3.3. Estimation and correction of the turbulent effect, and DEM generation

To remove the small-scale turbulent APS, the interferogram was segmented into consecutive subareas with size of 2×2 km^2. The response of $H(u, v)$ was calculated from the power spectrum of each subarea using Eq. (6) so that the bandwidth based on the local atmospheric signals was adaptively determined. The bandwidth of $L(u, v)$ was set as 0.5 cycle/km and $p = q = 1$ as described in Section 2.2.2. With $G(u, v)$, we estimated the turbulent APS in Fig. 3c on a subarea-by-subarea basis. The result is shown in Fig. 3d. Afterwards, by subtracting the estimated turbulent APS from the interferogram of Fig. 3c, we obtained the interferogram after the removal of both stratified and turbulent APS (Fig. 3e). Therefore, the remaining phase in Eq. (1) was topographic phase, $\phi_{\varepsilon topo}$.

Indeed, topographic details of the terrain with steep slopes were clearly depicted in Fig. 3e. This high-resolution interferogram can be used to create the high-resolution DEM.

Using the SRTM DEM data as a base reference, we re-scaled the elevation values within the high resolution DEM to the elevation data above the mean sea level. Fig. 3f shows the DEM in SAR azimuth and slant-range coordinates. Then, the DEM was geocoded and projected on to the WGS84/Universal Transverse Mercator (UTM) coordinate system of North zone 47 (Geudtner and Schwäbisch, 1996). The output cell spacing was set as 10 m in both Northing and Easting. A color-coded hill-shading image of the resulting DEM is shown in Fig. 4a. The glacial fluvial deposition was located at the northern portion of the area, while the rugged terrain of the Qilian Mountains remained in the south. The DEM might well depict the general topographic pattern in the area.

3.4. Assessment of the derived high-resolution DEM

The Chinese national 1:50,000 DEM was used in the assessment as reference by assuming it to be free of error. Due to different cell sizes, the InSAR-derived DEM was resampled to 25 m resolution. The residual after the differentiation between reference DEM and corrected InSAR-derived DEM is shown in Fig. 4b. 93.3% of cells were within the interval of ±10 m, which is within the vertical accuracy limits of the 1:50,000 DEM. The mean value and standard deviation (STDEV) of the residual were 1.1 m and 5.7 m, respectively. The STDEV can be taken as the root-mean-square error (RMSE) of the InSAR-derived DEM.

In comparison, the differentiation between the InSAR-derived DEM without atmospheric artifact correction and the 1:50,000 DEM has also been done. As shown in Fig. 4c, the spatial correlation pattern is mainly contributed by atmospheric artifacts. Moreover, the mean of residual increased to 1.7 m and STDEV to 13.6 m. There are only 54.7% of pixels within the interval of ±10 m accuracy limits. It is noteworthy that the assessment performed is just a preliminary analysis. Further assessment will be carried out if a superior DEM such as a LiDAR DEM is available. Nevertheless, the effectiveness of our APS removal approach has been verified, and a satisfactory high-resolution DEM in rugged terrain was created.

4. Discussion

In Eq. (7), p determines the relative proportion of $H(u, v)$ related to $L(u, v)$, and q represents the degree of smoothing of $H(u, v)$ within

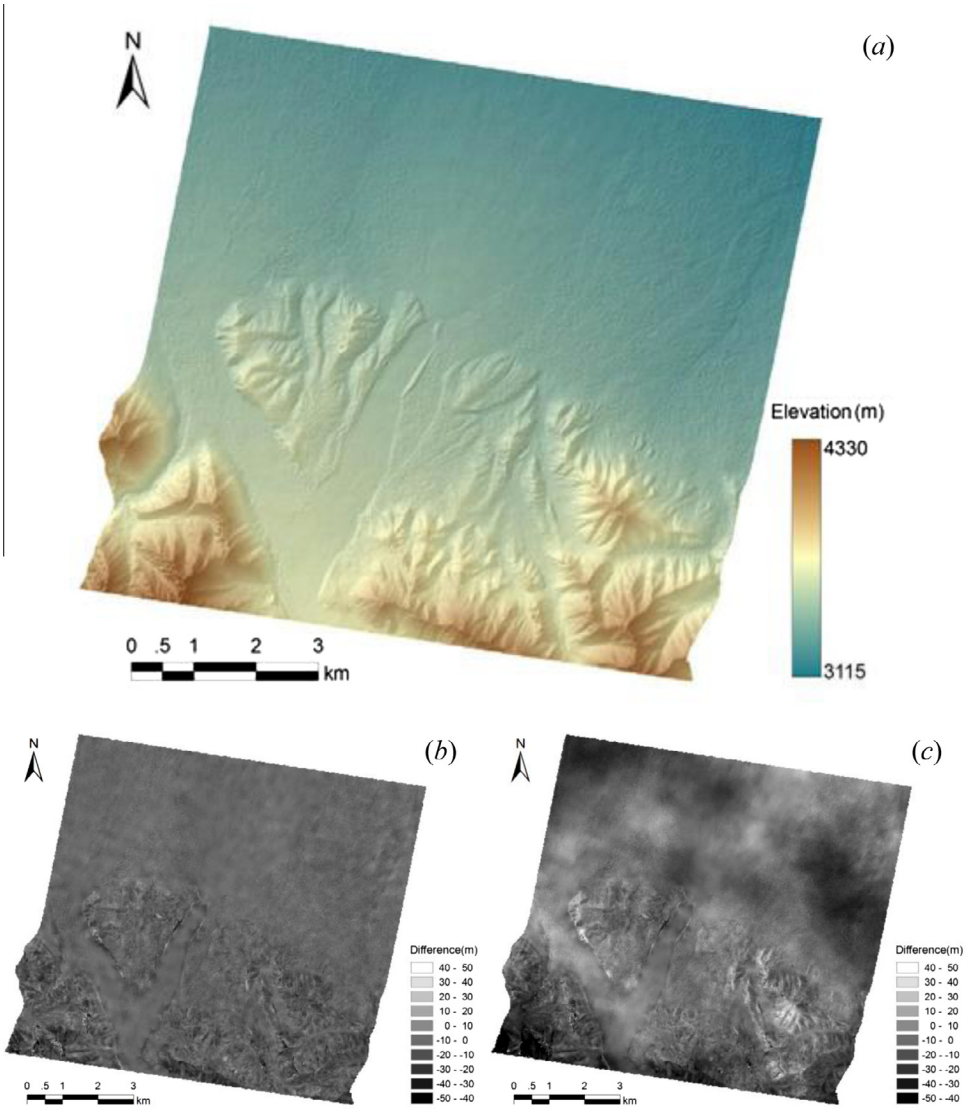

Fig. 4. (a) High-resolution InSAR DEM in UTM coordinate system. (b) InSAR DEM with atmospheric correction minus 1:50,000 national DEM, and (c) InSAR DEM without atmospheric correction minus 1:50,000 national DEM.

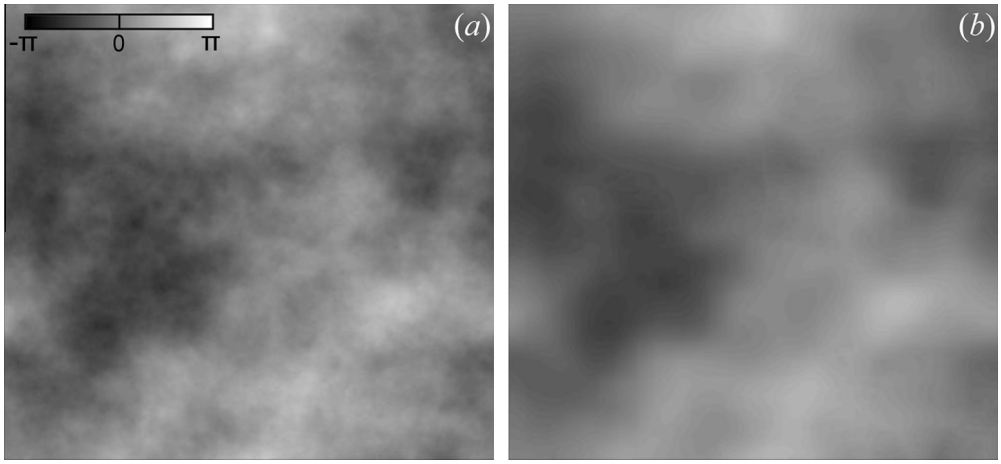

Fig. 5. (a) Simulated turbulent APS using a power spectrum of random numbers scaled with the power-law model. (b) Estimated turbulent APS at $p = 1.0$ and $q = 0.5$.

a subarea (Goldstein and Werner, 1998). p or q varies from 0 to 1. A high value of p or q means a large proportion or strong effect of smoothing, respectively. To determine the optimal combination of p and q values, we first simulated an interferogram that consists of turbulent APS and topographic phase. Such an interferogram could be considered equivalent to the one in Fig. 3c. A simulated APS has been generated and shown in Fig. 5a, which was using a power spectrum of uniformly distributed random numbers that was scaled with the empirical atmospheric model presented by Hanssen (2001). The phase could be characterized as random variation. To derive the interferogram that contains components of the simulated APS and topographic phase, the following four major steps have been done.

(i) simulating an interferogram from a DEM,
(ii) filtering the interferogram with a low-pass filter to obtain a low resolution one,
(iii) subtracting the interferogram of (ii) from that of (i), and
(iv) modulating the interferogram of (iii) with the simulated APS.

Then, $G(u, v)$ with different combinations of p and q was used to estimate the APS from the designed differential interferogram. The STDEV of the difference between the simulated APS and each estimated one has been computed. An optimal pair (p,q) was determined by minimization of the corresponding STDEV. In particular, 10 discrete values, i.e. 0.1, 0.2, $\cdots$, 1.0 were assigned to p and q, respectively. Therefore, 100 estimated APS were obtained by employing different combination of p and q. Then, the difference operation between each estimated APS in the set and the simulated APS was carried out, and the resulting STDEVs were analyzed to detect the minimum value. The optimized filter was found at $p = 1.0$ and $q = 0.5$ with a corresponding STDEV of 0.103 rad. The estimated APS is shown in Fig. 5b. However, we noted that although the maximum value of STDEV was 0.149 at $p = 0.1$ and $q = 1.0$, the majority of the values was not far away from 0.103 rad. In particular, with $p = q = 1.0$, the STDEV was 0.113 rad. The absolute difference between this STDEV and the smallest one was 0.010 rad. The relative difference was 0.010/0.103 or about only 9.7%. With the height ambiguity being −164 m in this study, this phase difference corresponds to a height change of approximately 0.26 m, which could be considered as small enough to be ignored in large-area topographic mapping.

To quantify whether substantial difference existed in the production of high resolution DEM with different pairs of p and q, we applied $G(u, v)$ with three pairs (p,q) of different values to the interferogram of Fig. 3c to estimate the turbulent APS and created three APS-corrected DEMs accordingly. For the first and second pairs, p was set as 1.0, while q was 0.5 and 1.0 respectively. For the third pair, p takes a zero value. For convenience, we named the three InSAR-derived DEMs as DEM A, DEM B and DEM C, separately. For each InSAR-derived DEM, a differencing operation between it and the reference 1:50,000 DEM was conducted, and the results were statistically tabulated in Table 1. Furthermore, STDEV of the differences for the three InSAR-derived DEMs were also given in Table 1.

We can learn from Table 1 that percentages within each interval for DEM A and DEM B are significantly higher than the corresponding one for DEM C. For example, the percentages of difference value $\leqslant$±5.0 m are 68.5% and 66.6% for DEM A and DEM B respectively, while for DEM C it is only 57.6%. A similar pattern shows up in the STDEV of the differences, for which an evidently larger standard deviation of 7.1 m for DEM C than those for DEM A and DEM B is observed. This comparison reveals that the adaptive component of the filter $G(u, v)$ plays a critical role in the compensation of small scale features or components of high spatial frequency after filtering by $L(u, v)$. Hence, this filter component should be included in the estimation of turbulent APS.

On the other hand, by comparing the results for DEM A and DEM B, we find that although the filter $G(u, v)$ with $p = 1.0$ and $q = 0.5$ shows slightly better performance than that with $p = q = 1.0$, the differences between them are actually subtle. Consequently, the choice of non-zero values for p and q only has a

Table 1
Cumulative percentages of height differences between three InSAR-derived DEMs and the reference 1:50,000 DEM.

InSAR-derived DEM	Cumulative percentage within					Standard deviation
	±1.0 m	±2.0 m	±3.0 m	±5.0 m	±10.0 m	
DEM A (at $p = 1.0$, $q = 0.5$)	14.8	30.7	45.8	68.5	93.6	5.6 m
DEM B (at $p = q = 1$)	14.5	29.5	44.1	66.6	93.3	5.7 m
DEM C (at $p = 0$)	12.4	24.7	36.6	57.6	87.3	7.1 m

minor impact on the turbulent APS estimation. In particular, with the combination of $p = q = 1.0$, we not only got a satisfactory result but also greatly simplified the process of DEM generation.

5. Concluding remarks

An effective but simple approach for the correction of both stratified and turbulent atmospheric effects on the high-resolution DEM generation has been developed. A high-resolution DEM was generated using only one pair of repeat-pass COSMO-SkyMed InSAR data. In the DEM derivation, the ground deformation was not considered due to the use of the InSAR pairs with a short temporal baseline of one or several days. In addition, the ionosphere effect on the radar signal was negligible due to the short wavelength of X-band adopted by the COSMO-SkyMed SAR sensor.

The major steps in producing the DEM are summarized as follows. An interferogram was created using the InSAR pair. With another interferogram simulated from the available SRTM DEM, a differential interferogram was obtained. A linear regression model was then established to use the differential interferogram and SRTM DEM to estimate the stratified APS. A combination of a low-pass and an adaptive filter was employed to further separate the turbulent APS. After the removal of both types of atmospheric effects, the high-resolution DEM could be produced from the refined topographic phase following the procedures of phase unwrapping, phase to height conversion, geocoding and projection. The effectiveness of the proposed approach has been demonstrated using a tandem-mode COSMO-SkyMed InSAR data pair covering a mountainous area in Northwestern China. The RMSE of the DEM resulting from this approach was only 5.7 m with reference to a standard Chinese national 1:50,000 DEM. In contrast, the RMSE obtained without consideration of atmospheric effect removal is 13.6 m.

Uniqueness of this approach includes letting $p = q = 1.0$ in the combined filter. A user could not only skip the empirical determination of p and q but also obtain satisfactory DEM. Thus, the procedure in the production of high-resolution DEM is simplified, which is of great advantage and potential. Another one is the combined use of one InSAR pair and a moderate-resolution reference SRTM DEM. The spatial resolution of the InSAR-derived DEM depends only on the resolution of the InSAR data. With the availability of the SRTM DEM, this method offers an alternative and fits niches where DEM of fine resolution is not likely available to the public or even does not exist. However, one caution should be kept in mind that the SRTM DEM was acquired in year 2000, and covered land surface between 60°S and 60°N latitudes on the Earth. When applying the algorithm to seismically active area or land outside the 60°S–60°N belt, the SRTM DEM could be out of date or unavailable. Replacing it with the recently released global ASTER GDEM, one could resolve the coverage issue. Furthermore, the ASTER sensor is operational, and multi-temporal ASTER GDEMs should be possible.

Acknowledgments

The anonymous reviewers are appreciated for their helpful comments and suggestions to improve the quality of this paper. This work was financially supported by the National Key Basic Research Program of China (Grant Nos. 2013CB733205 and 2013CB733204), National Natural Science Foundation of China (Grant Nos. 41271457 and 41021061), and Research Fund for the Doctoral Program of Higher Education of China (Grant No. 20110141110057). The authors thank the Italian Space Agency (ASI) and the Eastdawn Corp. for providing the COSMO-SkyMed SAR data pair and the National Geomatics Center of China for providing the Chinese national DEM.

References

Audet, C., Dennis, J.E.J.R., 2003. Analysis of generalized pattern searches. SIAM Journal on Optimization 13 (3), 889–903.
Brcic, R., Parizzi, A., Eineder, M., Bamler, R., Meyer, F., 2011. Ionospheric effects in SAR interferometry: an analysis and comparison of methods for their estimation. In: Jon Atli Benediktsson, Proc. IGARSS 2011, Vancouver, Canada, July 24–29, pp. 1497–1500.
Chaabane, F., Avallone, A., Tupin, F., Briole, P., Maître, H., 2007. A multitemporal method for correction of tropospheric effects in differential SAR Interferometry: application to the Gulf of Corinth earthquake. IEEE Transactions on Geoscience and Remote Sensing 45 (6), 1605–1615.
Covello, F., Battazza, F., Coletta, A., Lopinto, E., Fiorentino, C., Pietranera, L., Valentini, G., Zoffoli, S., 2010. COSMO-SkyMed: an existing opportunity for observing the Earth. Journal of Geodynamics 49 (3–4), 171–180.
Crosetto, M., 2002. Calibration and validation of SAR interferometry for DEM generation. ISPRS Journal of Photogrammetry & Remote Sensing 57 (3), 213–227.
Ding, X.L., Li, Z.W., Zhu, J.J., Feng, G.C., Long, J.P., 2008. Atmospheric effects on InSAR measurements and their mitigation. Sensors 8 (9), 5426–5448.
Doin, M.-P., Lasserre, C., Peltzer, G., Cavalié, O., Doubre, C., 2009. Corrections of stratified tropospheric delays in SAR interferometry: validation with global atmospheric models. Journal of Applied Geophysics 69 (1), 35–50.
Ferraiuolo, G., Meglio, F., Pascazio, V., 2009. DEM reconstruction accuracy in multichannel SAR interferometry. IEEE Transactions on Geoscience and Remote Sensing 47 (1), 191–201.
Ferretti, A., Prati, C., Rocca, F., 1999. Multibaseline InSAR DEM reconstruction: the wavelet approach. IEEE Transactions on Geoscience and Remote Sensing 37 (2), 705–715.
Ferretti, A., Prati, C., Rocca, F., 2001. Permanent scatterers in SAR interferometry. IEEE Transactions on Geoscience and Remote Sensing 39 (1), 8–20.
Geudtner, D., Schwäbisch, M., 1996. An algorithm for precise reconstruction of InSAR imaging geometry: application to flat-earth phase removal, phase to height conversion, and geocoding of InSAR-derived DEMs. In: Proc. EUSAR'96, Königswinter, Germany, March 26–28, pp. 249–252.
Goldstein, R.M., Werner, C.L., 1998. Radar interferogram filtering for geophysical applications. Geophysical Research Letters 25 (21), 4035–4038.
Hanssen, R., 1998. Atmospheric heterogeneities in ERS tandem SAR interferometry. Delft University Press, Delft, Netherland.
Hanssen, R.F., 2001. Radar Interferometry: Data Interpretation and Error Analysis. Kluwer Academic Publishers, Dordrecht, Netherland.
Hooper, A.J., 2006. Persistent scatterer radar interferometry for crustal deformation studies and modeling of volcanic deformation. PhD thesis, Stanford University, USA.
Knöpfle, W., Strunz, G., Roth, A., 1998. Mosaicking of digital elevation models derived by SAR interferometry. International Archives of Photogrammetry, Remote Sensing and Spatial Information Sciences 32 (4), 306–313.
Liao, M.S., Wang, T., Lu, L.J., Zhou, W.J., Li, D.R., 2007. Reconstruction of DEMs from ERS-1/2 Tandem data in mountainous area facilitated by SRTM data. IEEE Transactions on Geoscience and Remote Sensing 45 (7), 2325–2335.
Rodriguez, E., Morris, C.S., Belz, J.E., 2006. A global assessment of the SRTM performance. Photogrammetric Engineering & Remote Sensing 72 (3), 249–260.
Rufino, G., Moccia, A., Esposito, S., 1998. DEM generation by means of ERS Tandem data. IEEE Transactions on Geoscience and Remote Sensing 36 (6), 1905–1912.
Zebker, H.A., Rosen, P.A., Hensley, S., 1997. Atmospheric effects in interferometric synthetic aperture radar surface deformation and topographic maps. Journal of Geophysical Research 102 (B4), 7547–7563.